

# Controlling Umklapp scattering in bilayer graphene moiré superlattice

Mohit Kumar Jat<sup>1</sup>, Shubhankar Mishra<sup>1</sup>, Harsimran Kaur Mann<sup>1</sup>, Robin Bajaj<sup>1</sup>, Kenji Watanabe<sup>2</sup>, Takashi Taniguchi<sup>3</sup>, H. R. Krishnamurthy<sup>1</sup>, Manish Jain<sup>1</sup> and Aveek Bid<sup>1\*</sup>

<sup>1</sup>*Department of Physics,  
Indian Institute of Science,  
Bangalore 560012, India*

<sup>2</sup>*Research Center for Electronic and Optical Materials,  
National Institute for Materials Science,  
1-1 Namiki, Tsukuba 305-0044, Japan*

<sup>3</sup>*Research Center for Materials Nanoarchitectonics,  
National Institute for Materials Science,  
1-1 Namiki, Tsukuba 305-0044, Japan*

## Abstract

In this Letter, we present experimental findings on electron-electron scattering in a two-dimensional moiré heterostructure with tunable Fermi wave vector, reciprocal lattice vector, and band gap. We achieve this in high-mobility aligned heterostructures of bilayer graphene (BLG) and hBN. Around half-filling, the primary contribution to the resistance of BLG/hBN aligned superlattices arises from electron-electron Umklapp (U<sub>ee</sub>) scattering, making the resistance of graphene/hBN moiré devices significantly larger than that of non-aligned devices (where U<sub>ee</sub> is forbidden). We quantify the strength of the U<sub>ee</sub> scattering and find that it follows a universal scaling with Fermi energy and has a non-monotonic dependence on the charge carrier density. The U<sub>ee</sub> scattering is strongly electric field tunable and affected by layer-polarization of BLG. It has a strong particle-hole asymmetry – the resistance when the chemical potential is in the conduction band is significantly lesser than when it is in the valence band making the electron-doped regime more practical for potential applications.

## I. INTRODUCTION

In a Galilean-invariant electron liquid, normal electron-electron scattering does not cause a loss of the momentum imparted to the electrons by the driving electric field; consequently, it can not lead to electrical resistance. A realistic Fermi liquid is, however, not Galilean invariant – a finite coupling to an underlying lattice provides a mechanism for the momentum relaxation of the quasiparticles via the Umklapp process [1]. Umklapp electron-electron (U<sub>ee</sub>) scattering is the fundamental mechanism that allows momentum transfer from electrons to lattice and imparts electrical resistance to the metal [2–8]. In this process, the crystal lattice gives a momentum kick to a pair of interacting electrons, backscattering them to the other side of the Fermi surface. Their quasi-momentum is conserved, modulo a reciprocal lattice vector  $\mathbf{G}$ ,

$$\mathbf{k}_1 + \mathbf{k}_2 = \mathbf{k}_3 + \mathbf{k}_4 + \mathbf{G} \quad (1)$$

Here  $\hbar\mathbf{k}_{1,2}$  and  $\hbar\mathbf{k}_{3,4}$  are the initial and final quasi-momenta of the two electrons near the Fermi level, respectively, and  $\mathbf{G}$  is a non-zero reciprocal lattice vector of the crystal. This stringent

---

\* [aveek@iisc.ac.in](mailto:aveek@iisc.ac.in)

conservation constraint, coupled with the lack of tunability of the Fermi wave vectors, makes experimental identification of Uee processes in normal metals challenging [7–9]. Notable exceptions are heavy-fermionic systems whose large effective quasiparticle mass leads to an appreciable Uee-mediated resistance at very low temperatures ( $\approx 100$  mK) [10].

In the limit of nearly free electrons, one can view the Uee scattering as a two-stage process: In the first step, an electron-hole pair is excited into a virtual state by an electron, followed by the scattering of one of these particles by the periodic lattice potential. The temperature dependence of the Uee scattering process at a finite temperature is thus set by the size of the scattering phase space ( $\propto k_B T / E_F$ ) for each electron; only the quasiparticles residing within a width of order  $k_B T$  around the Fermi energy  $E_F$  can undergo binary collisions. Consequently, the Uee contribution to the sheet resistance in 2D goes as  $R_{\square Uee} = f_n T^2$  [11].  $f_n \propto E_F^{-2}$  is a material-dependent parameter [12–14].

Note, however, that Uee need not be the only source of  $T^2$ -resistivity in a material [13, 15–18]. A claim that the dominant source of scattering is the Uee process should be backed up by a (1) quantification of the prefactor  $f_n$ , (2) a demonstration of the scaling of  $f_n \propto E_F^{-2}$ , and (3) ruling out other competing mechanisms (e.g. electron-phonon scattering [18]) that can give  $T$ -dependent charge scattering.

Graphene-based moiré superlattices [4, 6, 19–25] provide a system with precise tunability of the reciprocal lattice vectors  $\mathbf{G}$  (via the twist angle between the constituent layers) and the Fermi wave vectors  $\mathbf{k}_F$  (by controlling the carrier density  $n$  through electrostatic gating). It thus provides a vast phase space in which Eqn. 1 may be satisfied, and the scaling of  $f_n$  versus  $E_F$  can be verified. Recent calculations (that treat both the electron-electron Coulomb interaction and the moiré superlattice potential perturbatively) predict that in aligned heterostructures of Bernal bilayer graphene (BLG) and hBN, Uee scattering processes should be the dominant source of resistance [5].

In this Letter, we experimentally verify that in high-mobility moiré superlattices of BLG and hBN, Uee is the dominant source of resistance near half-filling. Our studies show that the strength of Uee depends non-monotonically on the supermoiré period and charge-carrier density. This is at par with recent theoretical predictions [5] and in sharp contrast to observations in single-layer graphene-based superlattices [4]. We illustrate the tunable layer polarization of the moiré strength with carrier density  $n$  and displacement field  $D$ . Additionally, we demonstrate a strong particle-

hole asymmetry in the strength of the Uee process whose origin can be traced to the much larger probability of the back-scattering of holes than that of electrons [4]. Furthermore, we demonstrate the high tunability of Umklapp resistivity with an external vertical electric field, emphasizing the potential for precise control over the electronic properties of bilayer graphene superlattices. Finally, we show that these processes are completely absent in non-aligned devices.

## II. RESULTS AND DISCUSSION

High-quality hBN/BLG/hBN heterostructures were fabricated using the dry transfer technique (Supplementary Information, section S1) [26–28]. The top hBN was aligned at nearly zero degrees with BLG, and the bottom hBN was intentionally misaligned to a large angle to ensure that a moiré pattern forms only between top hBN and BLG (Fig.1(a)). The device is in hall bar geometry (Fig.1(b)) with dual gates to tune the carrier density  $n$  and the vertical displacement field  $D$  independently via  $n = [(C_{tg}V_{tg} + C_{bg}V_{bg})/e + n_r]$  and  $D = [(C_{bg}V_{bg} - C_{tg}V_{tg})/2 + D_r]$ . Here  $C_{bg}$  ( $C_{tg}$ ) is the back-gate (top-gate) capacitance, and  $V_{bg}$  ( $V_{tg}$ ) is the back-gate (top-gate) voltage.  $n_r$  and  $D_r$  are the residual number density and displacement field in the graphene due to impurities. The direction of the positive displacement field ( $D$ ) is marked schematically in Fig.1(a). In the main text, we provide the data for a device **M1** (with twist angle  $\approx 0^\circ$ ), unless otherwise mentioned. The data for another hBN/BLG/hBN superlattice device, **M2** (with twist angle  $\approx 0.26^\circ$ ), are presented in Supplementary Information. We also present data for a non-aligned hBN/BLG/hBN device (labeled **N1**) to compare the  $T$ -dependence of resistance between Uee-allowed (aligned devices) and Uee-forbidden (non-aligned devices) systems.

The measured longitudinal resistance  $R_{xx}$  on device **M1**, at 2K temperature shows a peak at the charge neutrality point (CNP),  $n_{CNP} = 0$  and moiré satellite peaks at  $n_M = \pm 2.30 \times 10^{16} \text{ m}^{-2}$  (Fig. 1(c)). The mobility at CNP is extracted to be  $350,000 \text{ m}^2\text{V}^{-1}\text{s}^{-1}$ . Quantum Hall measurements at a perpendicular magnetic field of  $B = 5 \text{ T}$  establish that both spin and valley degeneracies are lifted, indicating the high quality of the device (Supplementary Information, Section S5); these measurements are used to calibrate the values of  $C_{bg}$  and  $C_{tg}$ . The angle homogeneity of the device is ascertained by comparing the  $R_{xx}$  data measured in different configurations (Supplementary Information, section S2).

Our results for  $R_{xx}$  as a function of carrier density  $n$  and electric field  $D/\epsilon_0$ , shown in Fig.1(d)



ascertain that the values of the moiré gap in carrier density  $n_M$  are independent of the applied electric field. The plot can be divided into four quadrants labeled I-IV. In quadrants I ( $n = +ve$ ,  $D/\epsilon_0 = +ve$ ) and III ( $n = -ve$ ,  $D/\epsilon_0 = -ve$ ), at a finite  $D$ , the electronic states of the carriers have higher weights (marked with a red color oval) in the bottom layer of BLG (away from moiré interface) and lower weights (marked with a blue color oval) in the top layer of BLG (close to moiré interface) – this leads to the suppression of moiré effects and low resistance value of satellite peak in these quadrants. The opposite effect is seen in quadrants II ( $n = +ve$ ,  $D/\epsilon_0 = -ve$ ) and IV ( $n = -ve$ ,  $D/\epsilon_0 = +ve$ ), the electronic states of the carriers have higher weights in the top layer of BLG (close to moiré interface) leading to the enhancement of moiré effects and higher resistance of the satellite peaks in these quadrants. Later in this Letter, we explore the consequences of this displacement-field induced layer polarization on Uee scattering.

The moiré periodicity of the system is estimated from Brown-Zak oscillation measurements at  $T = 100$  K (Fig.1(e)). Thermal broadening smears out Landau oscillations at this elevated temperature, and only Bloch oscillations survive [19, 29–31]. A Fourier spectrum of the oscillations yields the inverse periodicity or the ‘frequency’ of the oscillations to be  $B_f = 24.2$  T (Fig.1(f)). Observation of only a single frequency rule out the double alignment of the BLG with hBN [19, 32]. Using the relation  $S = h/eB_f$  ( $S$  being the real space area of the moiré superlattice cell,  $h$ : Planck’s constant,  $e$ : electronic charge), the moiré wavelength is calculated to be  $\lambda = 14$  nm and the carrier density corresponding to filling the bands just up to the moiré gaps is  $4/S = 2.30 \times 10^{16} \text{ m}^{-2}$ ; the factor of 4 arises from the two-fold spin-and valley-degeneracy of graphene. This value of carrier density matches  $n_M$  exactly, validating the number density corresponding to the moiré gap obtained from zero-magnetic field  $R_{xx}$  measurements. The twist angle between BLG and hBN corresponding to this moiré wavelength is approximately  $0^\circ$  indicating near-perfect alignment between the top hBN and the BLG.

Fig. 2(a) shows the plots of the zero-magnetic field longitudinal sheet resistance  $R_\square = R_{xx}w/l$  ( $w$  and  $l$  are the width and length of the channel respectively with  $w/l = 1.5$ ) versus the moiré band filling fraction  $n/n_0$  over a temperature range  $5 \text{ K} < T < 300 \text{ K}$  at zero displacement field. Here,  $n_0 = 1/A = n_M/4$  is the carrier density at one-fourth filling of the moiré band. With increasing temperature, one notices a sharp increase in  $R_\square$  around  $n/n_0 = -2$ ; this feature is completely absent in non-aligned BLG devices (Supplementary Information, section S3). As we establish below, this rapid increase in  $R_\square$  with  $T$  arises from the Umklapp scattering in the device.

At  $T = 0$ ,  $U_{ee}$  is suppressed, and the resistivity is dominated by disorder scattering [12]. To mitigate the effect of static disorder scattering, we henceforth focus on  $\Delta R_{\square}(T) = R_{\square}(T) - R_{\square}(5 \text{ K})$ . In Fig. 2(b) we plot  $\Delta R_{\square}/T^2$  versus  $n/n_0$  over a temperature range from 30 K to 110 K – the data at all temperatures collapse onto a single curve in the filling fraction range  $-2 \leq n/n_0 \leq -1$  (marked by the dotted ellipse) showing that  $\Delta R_{\square} \propto T^2$  over this range. The linearity of the plots of  $\Delta R_{\square}$  versus  $T^2$  in this carrier density regime persists till about  $T \simeq 110 \text{ K}$ , establishing  $U_{ee}$  scattering as the source of resistance (Fig. 2(c)). This temperature is of the order of the Bloch-Grüneisen temperature in graphene. Above this  $T$ , electron-phonon scattering starts becoming the dominant source of resistance, and the quadratic relation between  $\Delta R_{\square}$  and  $T$  breaks down [33–35]. Fig. 2(d) shows a comparison of  $\Delta R_{\square}$  for the three devices – the strong quadratic  $T$ -dependence seen in aligned devices is completely absent in the non-aligned device where  $U_{ee}$  is forbidden from phase-space arguments.

To understand the number density limits over which Umklapp processes are seen, recall that at very low  $n/n_0$ , transport in graphene is dominated by electron-hole puddles [33, 36, 37]; this gives a practical lower bound of  $n/n_0$  at which e-e scattering is detectable [5]. A more accurate lower limit is obtained by the constraint mentioned earlier that the  $U_{ee}$  process imposes the Fermi wave vector  $k_F$  due to Eqn. 1, this sets a lower bound on  $|n/n_0|$  equal to  $\pi/(2\sqrt{3}) = 0.91$ . (see Supplementary Information, S4). At the other extreme, at high number densities, one begins to encounter electron-hole scattering processes at the principal mini band edges because of the moiré induced van-Hove singularity (Fig.3(b)), which masks the Umklapp scattering process [5].

Before proceeding further, we eliminate the other probable causes that are known to lead to a  $T^2$ -dependence of the resistance. In a system with different carrier types/masses (as is the case near the primary and secondary gaps or van Hove singularities), the transfer of momentum between the two carrier reservoirs can lead to a resistivity with  $T^2$  dependence [38–40]. This consideration guides us to avoid filling fractions that lead to Fermi levels close to these regions of the moiré bands and confine our analysis to the filling fraction range  $-2 \leq n/n_0 \leq -1$ , as shown in Fig.3(b). We note that, in low-mobility dilute alloys, the thermal motion of impurity ions can also give rise to a  $T^2$ -dependent resistance [41]; this scenario does not apply to our high-mobility heterostructures.

We now quantitatively analyze our data in terms of the  $U_{ee}$  scattering model. For two-dimensional

systems:

$$R_{\square} = \frac{\hbar}{e^2} \left( \frac{k_B}{E_F} \right)^2 (k_F l_{\sigma}) \times T^2 = f_n T^2 \quad (2)$$

with,

$$f_n = \frac{\hbar}{e^2} \left( \frac{k_B}{E_F} \right)^2 (k_F l_{\sigma}) \quad (3)$$

Here,  $R_{\square}$  is the sheet resistance.  $l_{\sigma}$  is a phenomenological material-dependent length parameter whose magnitude is related to the microscopic details of momentum loss [12]. In low-density materials,  $l_{\sigma}$  is of the order of the Fermi wavelength [13]. Fig.3(a) plots  $l_{\sigma}$  versus the moiré band filling factor at  $T = 60$  K; the values match extremely well with those obtained previously for low-density materials [13]. Note that  $l_{\sigma}$ , and by extension  $f_n$ , has a non-monotonic dependence on  $n$  in agreement with theoretical predictions for BLG/hBN moiré superlattice [5].

To further emphasize the universality of the value of  $f_n$ , in Fig.3(c), we plot  $A = f_n t$  ( $t = 0.8$  nm is the thickness of BLG) as a function of the Fermi energy  $E_F$  along with the compilation of data on several different materials [12]; we find that our data lie perfectly on the modified version of the Rice-Kadowaki-Woods scaling plot [13, 14].

Having established Uee as the source of quasiparticle scattering in bilayer graphene/hBN moiré near half-filling ( $n/n_0 = -2$ ), we now shift our focus on the effect of inter-layer potential asymmetry (tuned using  $D$ ) on the Umklapp scattering in the quadrant III and IV of Fig. 1(d). Fig. 4(a) plots  $\Delta R_{\square}(n/n_0 = -2)$  versus  $T^2$  for several different values of  $D/\epsilon_0$ . We find that the temperature exponent of the resistance  $\alpha = d \ln(\Delta R_{\square}) / d \ln(T) \approx 2$  for  $-0.3 \text{ V/nm} \leq D/\epsilon_0 \leq 0.3 \text{ V/nm}$  (Fig. 4(b)). In this range of  $D/\epsilon_0$ , we find a substantial increase in the scattering strength with increasing  $D/\epsilon_0$  in conformity with theoretical predictions [5] (Fig. 4(c)). Fig. 4(d) plots  $f_n(D)$  versus  $D/\epsilon_0$  over the temperature range 60 K– 100 K. These curves collapse on top of each other with  $f_n$  growing quadratically with  $D/\epsilon_0$ . Note the asymmetry of  $f_n$  under sign-reversal of  $D/\epsilon_0$ . To understand this, we recall that the sign of layer polarization in BLG is opposite for opposite signs of  $D$ . Thus at negative  $n$ , a positive (negative)  $D$ -field shifts the weight of the low-energy electronic states towards (away from) the top layer of the BLG (that forms the moiré with the hBN) leading to the asymmetric dependence of  $f_n$  on the sign of  $D$  [5].

With further increase in the displacement field,  $\alpha$  deviates from two, indicating a suppression of Umklapp processes for  $|D/\epsilon_0| > 0.3 \text{ V/nm}$ . We do not have a clear understanding of the

origin of this. One plausible reason can be that at large  $D$ , the trigonal warping becomes strong, severely limiting the phase space over which Eqn. 1 may be satisfied [42]. A related effect of the trigonal warping is the formation of overlapping electron-hole bands at certain number densities – the scattering between thermally excited electrons and holes then masks Uee processes [5, 42]. A second possible cause of the suppression of Uee at high  $D$  can be the strong modification of the BLG band by the displacement field (this includes layer-polarization, the opening of a band gap, and enhanced trigonal warping) leading to strong Zitterbewegung, which becomes the relevant scattering mechanism at large  $|D|$  [43]. Further experimental and theoretical studies are required to verify if any of these is indeed the cause for the suppression of Umklapp scattering with increasing  $D$ .

### III. CONCLUSION

To conclude, our experiments unequivocally establish Umklapp scattering to be the leading source of resistance in hBN/BLG superlattices in certain filling fraction ranges. Our findings on hBN/BLG superlattice differ from recent studies on hBN/SLG superlattice [4] in several significant aspects. In SLG hBN moiré  $R_{Uee}$  increases monotonically with increasing superlattice period and charge carrier density [4]. In contrast,  $R_{Uee}$  in BLG moiré superlattice is predicted to have a non-monotonic dependence on both superlattice period and  $n$  [5]. In this Letter, we have experimentally verified these predictions. Additionally, bilayer-based systems provide strong electric field tunability of the band gap and layer polarization and thus have an enormous scope for room-temperature applications [44–49]. We have shown that the strength of Uee increases rapidly with the increasing strength of the displacement field; this fact must be factored in when designing any  $D$ -field controlled superlattice device architectures.

With the presently available technology, the best quality BLG field effect devices are formed when encapsulated between a crystalline insulator, like hBN [50–52]. As the growth of graphene in hBN leads to aligned layers [53–55], it is imperative to understand the significant sources of Joule heating in such systems for optimal room-temperature operations. Our present study achieves this and should motivate further studies in related systems like twisted bilayer graphene and twisted bilayers of transition metal dichalcogenides.

#### **IV. ACKNOWLEDGMENT**

A.B. acknowledges funding from U.S. Army DEVCOM Indo-Pacific (Project number: FA5209 22P0166) and Department of Science and Technology, Govt of India (DST/SJF/PSA-01/2016-17). M.J. and H.R.K. acknowledge the National Supercomputing Mission of the Department of Science and Technology, India, and the Science and Engineering Research Board of the Department of Science and Technology, India, for financial support under Grants No. DST/NSM/R&D\_HPC Applications/2021/23 and No. SB/DF/005/2017, respectively. M.K.J. and R.B. acknowledge the funding from the Prime Minister's research fellowship (PMRF), MHRD. S.M. acknowledges the funding from the National post doctoral fellowship (N-PDF), SERB. K.W. and T.T. acknowledge support from the JSPS KAKENHI (Grant Numbers 21H05233 and 23H02052) and World Premier International Research Center Initiative (WPI), MEXT, Japan.

#### **AUTHOR CONTRIBUTIONS**

M.K.J., S.M., H.K.M., and A.B. conceived the idea of the study, conducted the measurements, and analyzed the results. T.T. and K.W. provided the hBN crystals. R.B., M.J., and H.R.K. developed the theoretical model. All the authors contributed to preparing the manuscript.

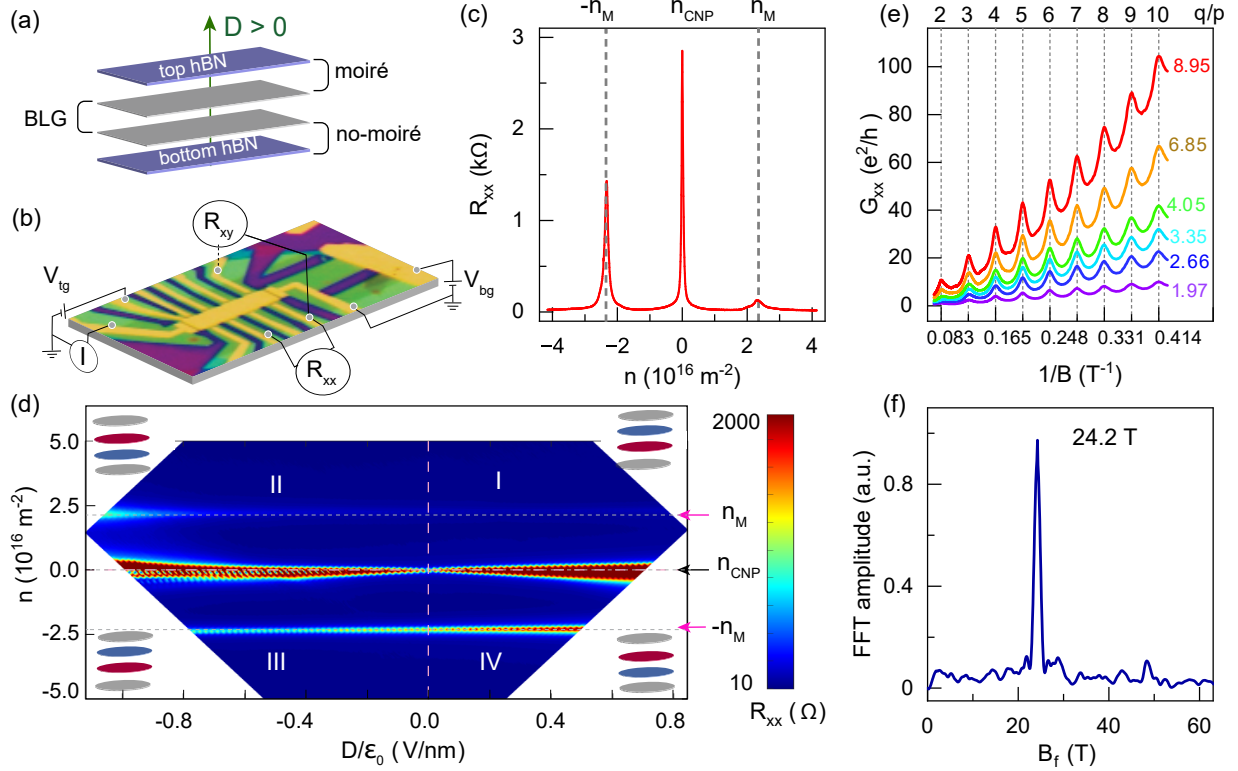


Figure 1. **Characteristics of the moiré device M1.** (a) Schematic of the device layers, indicating moiré (no-moiré) superlattice formation between top hBN (bottom hBN) and the BLG. (b) An optical image of the device labeled with the measurement configuration. (c) Plot of the longitudinal resistance  $R_{xx}(B = 0)$  at  $T = 2\text{K}$  as a function of  $n$ . Dotted gray lines mark the moiré satellite peaks with carrier density  $n_M = \pm 2.30 \times 10^{16} \text{ m}^{-2}$ . (d) 2D map of  $R_{xx}$  as a function of  $n$  and  $D$ . Labels I-IV mark the four quadrants in the  $n - D$  plane. The four insets show schematically the charge distribution in the two layers of BLG in these four regimes at high  $D$ . The red- and blue-filled ovals indicate the two layers that form the BLG. The red ovals indicate the layer with higher weights of the electronic states of the carriers while blue-filled ovals indicate the layer that has a lower weight of the electronic states. The upper bound on  $R_{xx}$  is set to be  $2 \text{ K}\Omega$  for better visibility of the satellite peak (for the complete data, see Supplementary Materials Section S2). (e) Plot of Brown Zak oscillations  $\Delta G_{xx}$  versus  $1/B$  for different carrier densities (units of  $10^{16} \text{ m}^{-2}$ ) measured at  $T = 100 \text{ K}$ . (f) The Fourier spectrum of the Brown Zak oscillations measured at  $n = 4.05 \times 10^{16} \text{ m}^{-2}$  shows a single prominent peak at  $B_f = 24.2 \text{ T}$ .

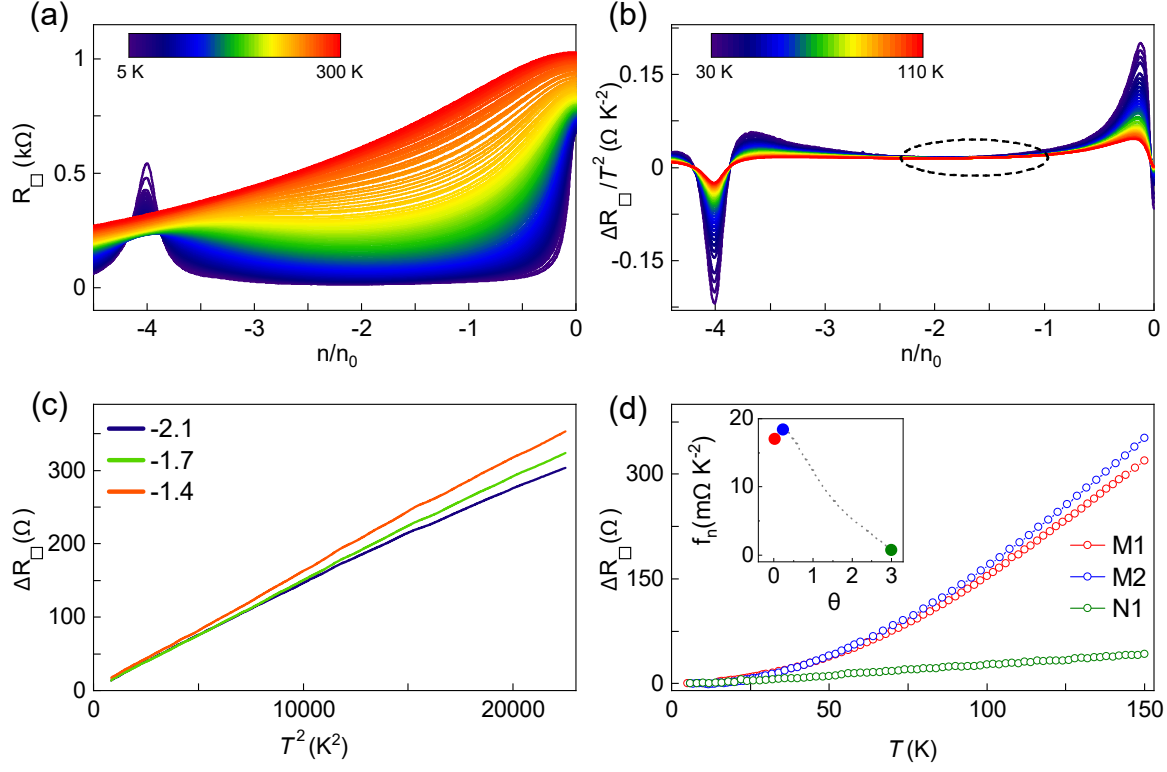


Figure 2. **Umklapp scattering at  $D/\epsilon_0 = 0$  V/nm.** (a) Plot of sheet resistance  $R_{\square}$  as a function of filling fraction  $n/n_0$  over a range of temperature from 5 K (blue) to 300 K (red). (b) Plot of  $\Delta R_{\square}/T^2 = (R_{\square}(T) - R_{\square}(5K))/T^2$  versus  $n/n_0$  over a range of temperature from 30 K (blue) to 110 K (red). The dotted ellipse marks the region where Umklapp is the dominant scattering mechanism. The negative value of  $\Delta R_{\square}/T^2$  around  $n/n_0 = -4$  is a consequence of the fact that at these number densities,  $R_{\square}$  decreases with increasing  $T$ . (c) Plot of  $\Delta R_{\square}$  as a function of  $T^2$  for three different values of  $n/n_0$ . (d) Comparison of the plots of  $\Delta R_{\square}$  versus temperature for two aligned devices (**M1** and **M2**) and the non-aligned device **N1**. Inset: Non-monotonic dependence of  $f_n$  on the moiré twist angle.

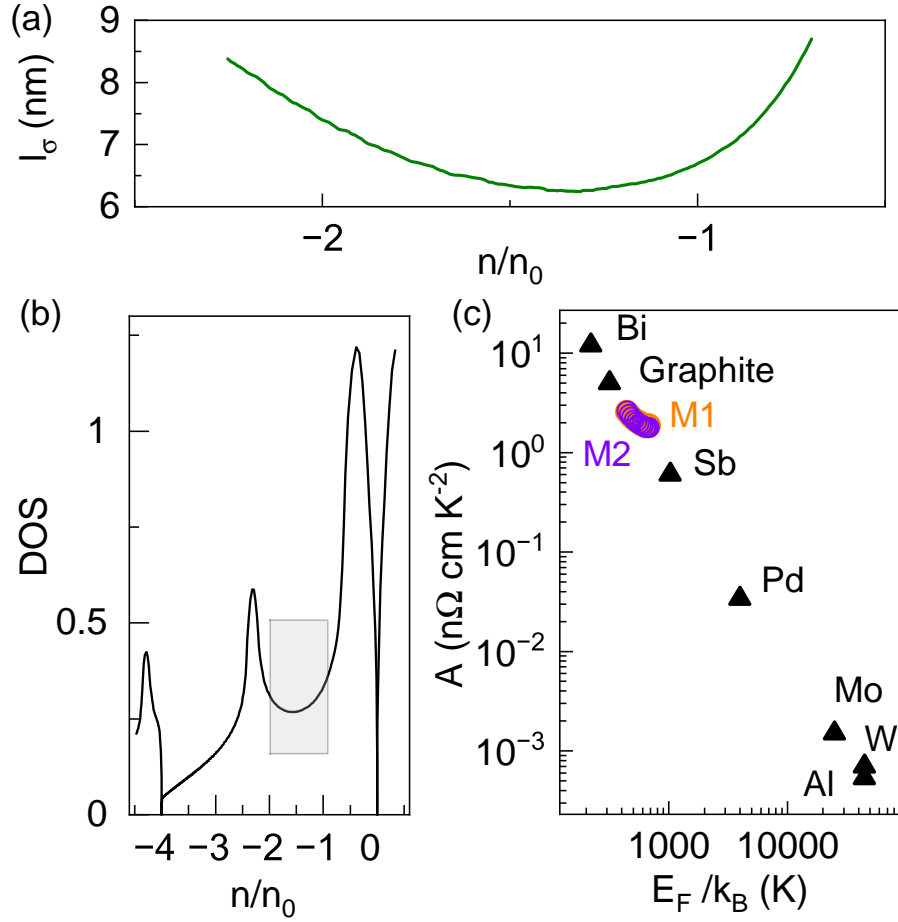


Figure 3. **Universal scaling of Umklapp scattering** (a) Plot of  $l_\sigma$  versus  $n/n_0$ . (b) Plot of the calculated density of states (DOS) versus  $n/n_0$ . The shaded area marks the number density range, away from band edges and van Hove singularities, where Uee processes can be unambiguously detected. (c) Plot of  $A = f_n t$  versus  $E_F/k_B$ . The open circles are the data from the current study on the two BLG/hBN moiré devices. The filled triangles are the data from Ref [12].



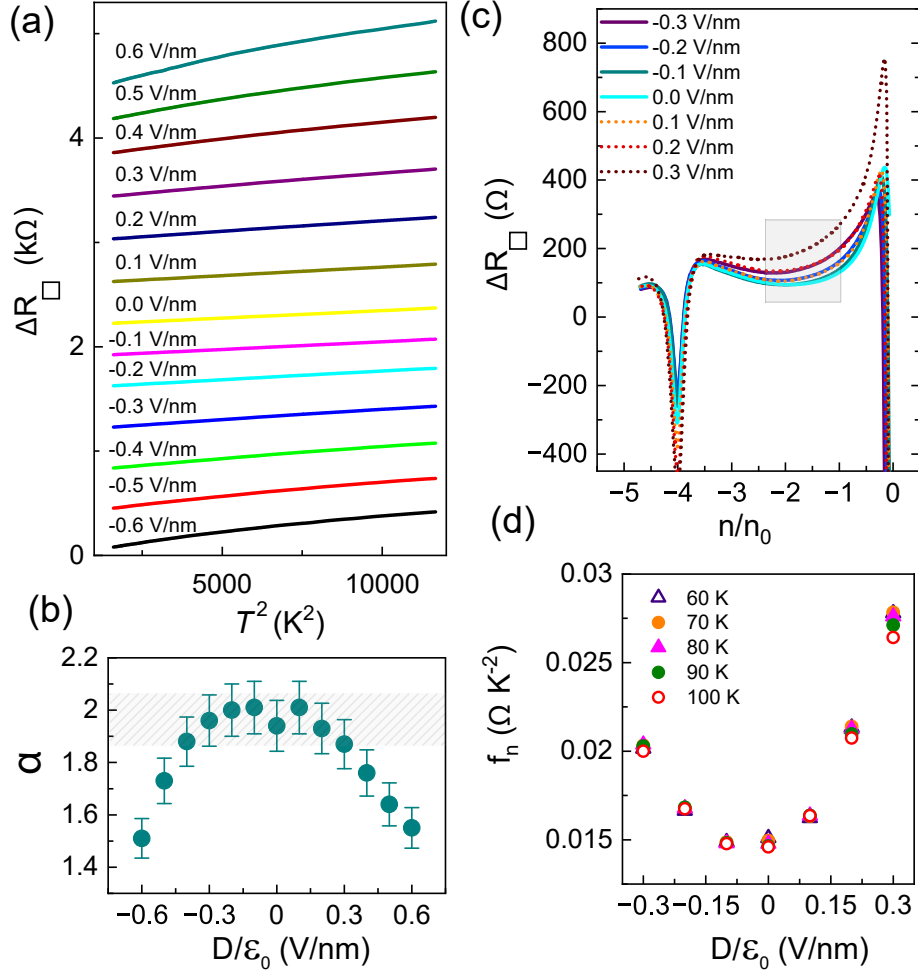


Figure 4. **Electric field dependence of Umklapp scattering** (a) Plots of  $\Delta R_{\square}$  versus  $T$  for different values of  $D/\epsilon_0$ , the data are for  $n/n_0 = -2$ . The numbers on the plots are values of the  $D/\epsilon_0$ . The data have been vertically offset for clarity. (b) Plot of the resistance exponent  $\alpha$  versus  $D/\epsilon_0$  at  $n/n_0 = -2$ . (c) Plot of  $\Delta R_{\square}$  versus filling fraction  $n/n_0$  at temperature  $T = 80$  K for different values of  $D/\epsilon_0$ . (d) Plots of  $f_n$  versus  $D/\epsilon_0$  at a few representative values of  $T$ .

## SUPPLEMENTARY MATERIALS

### S1. DEVICE FABRICATION

The hBN encapsulated bilayer graphene (BLG) devices were fabricated using the dry transfer technique [26–28]. Initially, BLG and hBN flakes were mechanically exfoliated onto a Si/SiO<sub>2</sub> substrate. BLG flakes were first identified with optical contrast and later confirmed with Raman spectra (Fig. S1). hBN flakes of thickness ranging from 25 – 30 nm were used in fabrication, and their thickness uniformity was confirmed using an AFM.

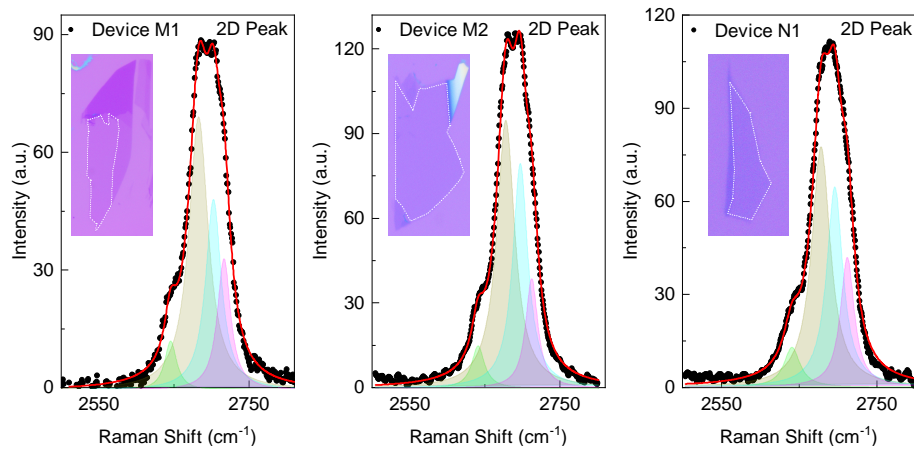


Figure S1. **Raman spectra of BLG flakes.** Plots of the 2D Raman peak of the bilayer graphene used to fabricate devices (a) **M1**, (b) **M2**, and (c) **N1**. The black-filled circles are the experimentally measured Raman spectra. The red solid line is cumulative of the four Lorentzian fitted to it; the four Lorentzian are also individually shown. The insets show the optical images of the BLG flakes; the shaded region marks the bilayer graphene used in device fabrication.

To make BLG-hBN single-moiré devices (devices **M1** and **M2**), the top hBN sharp edge was aligned with the sharp edge of BLG at nearly zero degrees, facilitating a moiré between BLG and the top hBN layer. The bottom hBN edge was intentionally misaligned with BLG to prevent any moiré superlattice formation between BLG and the bottom hBN layer.

In the case of a non-moiré device (**N1**), hBN was misaligned with both the bottom hBN and top hBN layers to prevent any moiré superlattice formation. Electrical contacts were patterned through lithography, etched with a mixture of CHF<sub>3</sub> (40 sscm) and O<sub>2</sub> (10 sscm), and contacts deposited with Cr/Pd/Au with thickness 5/12/55 nm to form 1D contact with BLG. The device was etched

in Hall bar geometry. Finally, The top gate was patterned through lithography, and a metal gate was deposited. Having dual gates in the devices gives control in tuning the system's carrier density and displacement field independently.

## S2. TWIST ANGLE ESTIMATION

Fig. S2 shows the plot of longitudinal resistance  $R_{xx}$  versus carrier density  $n$  for devices **M1** and **M2** measured for different pairs of voltage leads at  $T = 2\text{K}$  temperature. The resistance peak at  $n = 0$  originates from the charge neutrality point of the BLG. The resistance peak at  $n_{M1} = -2.30 \times 10^{16}\text{m}^{-2}$  ( $n_{M2} = -2.49 \times 10^{16}\text{m}^{-2}$ ) for device **M1** (**M2**) is a consequence of all levels up to the moiré gap getting filled at this carrier density. The independence of the carrier density at which the moiré gap emerges, regardless of the voltage probes used for the measurements (indicated with dotted lines), confirms the angle homogeneity in the devices. Further, Fig. S2(c) also illustrates that the carrier density corresponding to the moiré gap is independent of the applied displacement field.

The moiré wavelength is estimated using the relation [19, 24, 56]:

$$\lambda^2 = \frac{8}{\sqrt{3}n_M} \quad (\text{S1})$$

We find  $\lambda_1 = 14\text{ nm}$  for device **M1** and  $\lambda_2 = 13.64\text{ nm}$  for device **M2**.

We rule out dual-alignment of the BLG with both top - and bottom-hBN [19, 32] through measurements of the Brown-Zak oscillations of conductance at  $T = 100\text{ K}$ . At these elevated temperatures, landau levels get smeared out, and only the magnetotransport oscillations from the recurring Bloch states in the superlattice survive, and are shown in Fig.1(e) of the main text for device **M1** and in Fig. S3(a) for device **M2**. The periodicity of these oscillations is independent of the carrier density. The fast Fourier transform of these oscillations yields a single “frequency”  $B_f = 24.2\text{ T}$  ( $B_f = 25.7\text{ T}$ ) for device **M1** (**M2**), limiting the possibility of supermoiré in the system. We note that a single Brown Zak oscillation frequency can also occur if the two twist angles between the top hBN and BLG and that between the BLG and bottom hBN are identical; given that we intentionally misaligned the bottom hBN by a large angle, we rule out this scenario.

The frequency  $B_f$  is related to the real-space area  $S$  of the moiré unit cell by  $B_f = \phi_0/S$ , where  $\phi_0 = h/e$  is the flux quantum [24, 29, 31, 57]. Using the relation  $\lambda = \sqrt{(2S/\sqrt{3})}$ , we estimate

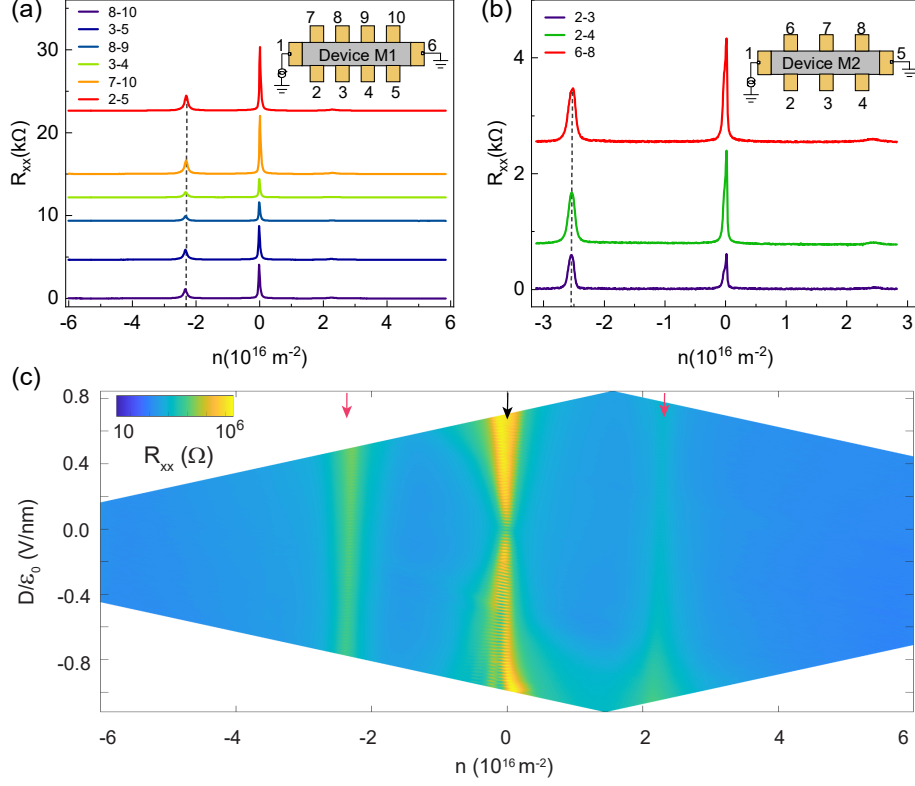


Figure S2. **Twist angle homogeneity of the moiré device.** (a) Plot of longitudinal resistance  $R_{xx}$  as a function of carrier density  $n$  measured at  $T = 2 \text{ K}$  for several configuration for device **M1**. The vertical dashed line marks the carrier density at which the secondary moiré gap emerges. The current was sourced between contacts 1 and 6. The numbers in the legend are the pairs of contacts used as voltage probes for the 4-probe measurement. (b) Same as in (a) for device **M2**. For both devices, the carrier density of the secondary moiré gap remains consistent across different configurations, illustrating the angle homogeneity within the devices. The plots are vertically offset for clarity. (c) 2D Plot of  $R_{xx}$  in the carrier density and the electric field  $D/\epsilon_0$  plane. The magenta (black) arrows mark the position of the moiré gap (CNP), illustrating that the position of the moiré gaps is independent of the applied perpendicular electric field.

$\lambda_1 = 14 \text{ nm}$  (for device **M1**) and  $\lambda_2 = 13.64 \text{ nm}$  (for device **M2**). These values match exactly with the moiré wavelength extracted from resistance versus carrier density response.

We estimate the twist angle magnitude between BLG and hBN using the relation [58, 59]:

$$\lambda = \frac{(1 + \epsilon)a}{[\epsilon^2 + 2(1 + \epsilon)(1 - \cos(\theta))]^{1/2}} \quad (\text{S2})$$

Here  $a = 0.246 \text{ nm}$  is the lattice constant of graphene,  $\epsilon = 0.018$  is the lattice mismatch between the hBN and graphene, and  $\theta$  is the relative twist angle between hBN and BLG. We find the twist

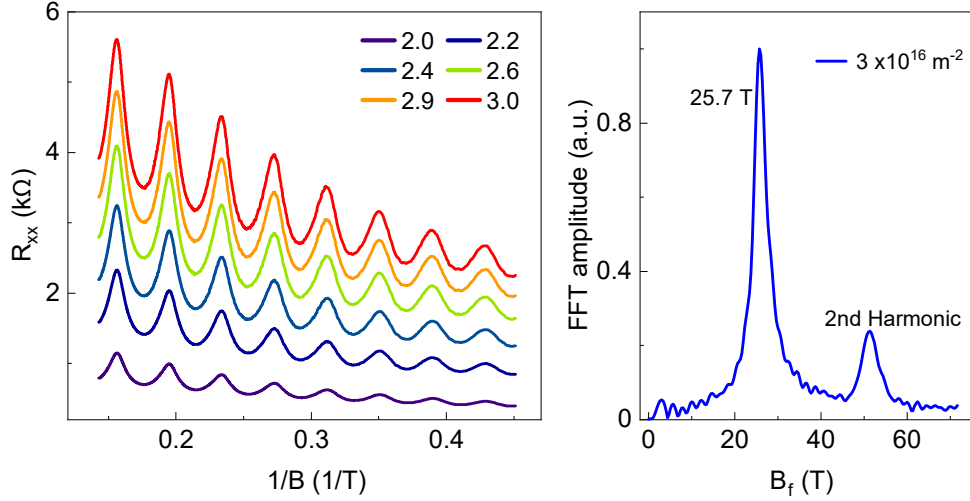


Figure S3. **Brown-Zak Oscillations of the moiré device M2.** (a) Plot of Brown Zak oscillations  $R_{xx}$  versus  $1/B$  at a few representative values of  $n$  measured at  $T = 100$  K. The legends in the plot indicate the carrier density in units of  $10^{16} \text{ m}^{-2}$ . The data are vertically offset for clarity. (b) The Fourier spectrum of the Brown Zak oscillations measured at  $n = 3 \times 10^{16} \text{ m}^{-2}$ . The peak at 25.7 T corresponds to moiré wavelength of 13.64 nm.

angle between the BLG and hBN to be  $\theta_{M1} = 0^\circ$  ( $\theta_{M2} = 0.26^\circ$ ) for device **M1** (**M2**).

### S3. COMPARISON OF SHEET RESISTANCE BETWEEN MOIRÉ AND NON MOIRÉ DEVICE

Fig. S4(a) shows the longitudinal sheet resistance versus carrier density response for device **M2** over a range of temperatures. The Umklapp electron-electron scattering dominated region is marked with dotted rectangles. The hole side (marked with an orange rectangle) shows a significantly larger strength of umklapp strength than the electron side (marked with a black rectangle). Fig. S4(b) plots the sheet resistance versus  $T^2$  to better show this electron-hole asymmetry over a range of  $n/n_0$ . The dotted orange (black) line shows a guiding straight line for holes (electrons) type carriers. This large asymmetric strength origin can be attributed to the much larger probability of the back-scattering of holes than that of electrons [4].

The  $T$ -dependence of the sheet resistance in non-aligned device **N1** are plotted in Fig. S4(c) for comparison. The data in the non-aligned device differ from that of **M1** and **M2** in three important aspects:

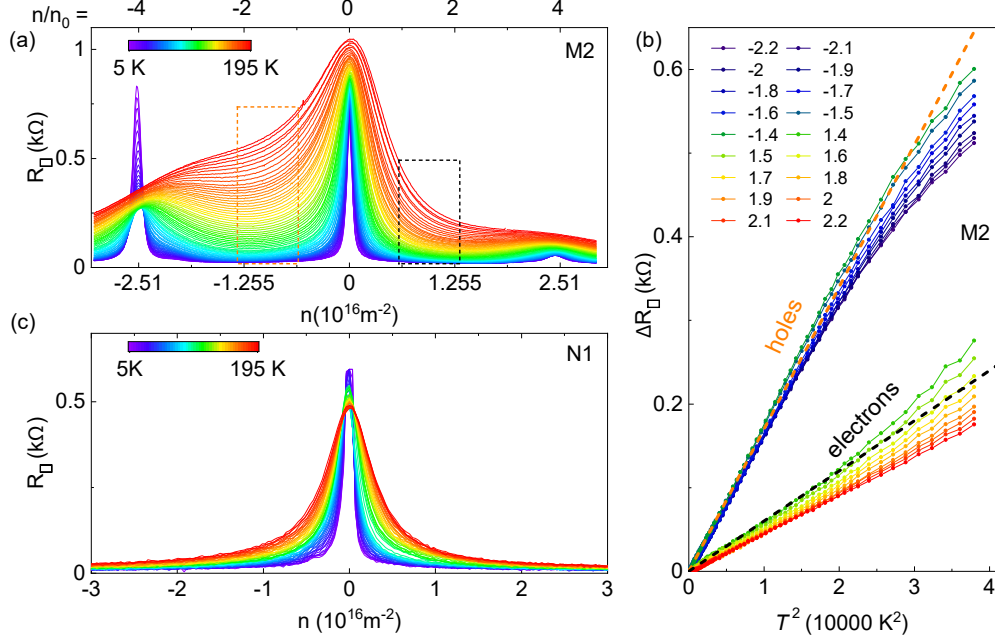


Figure S4. **Electron-Hole asymmetry of the moiré device and comparison with non-moiré device.** (a) Plot of longitudinal sheet resistance  $R_{\square}$  as a function of filling fraction  $n/n_0$  over a range of  $T$  from 5 K (blue) to 195 K (red). The measurements were done with  $B = 0$  and  $D = 0$ . The dotted rectangles mark the regions where Umklapp is the dominant scattering mechanism. The plot illustrates the particle-hole asymmetry in the strength of  $U_{ee}$ . (b) Plots of  $\Delta R_{\square}$  versus  $T^2$  at a few representative filling fractions ( $n/n_0$ ) for electron and hole doping. The numbers in the legend are the values of  $n/n_0$ . The dotted lines are linear fits to the data at  $n/n_0 = \pm 1.4$ . (c)  $T$ -dependence of  $R_{\square}$  for the non-aligned device **N1** – note the absence of the large resistance enhancement with  $T$ , as seen in the case of the moiré devices.

1. The large increase in sheet resistance seen in **M1** and **M2** with increasing  $T$  is conspicuously absent in the non-aligned device **N1**.
2. A  $T^2$ -dependence of the sheet resistance is not observed for the device **N1** (Fig.2(d) of the main manuscript). This is expected since, in a non-aligned device, Umklapp scattering is forbidden [5].
3. In contrast to that of **M1** and **M2**, the electron-hole asymmetry in sheet resistance is absent for device **N1**.

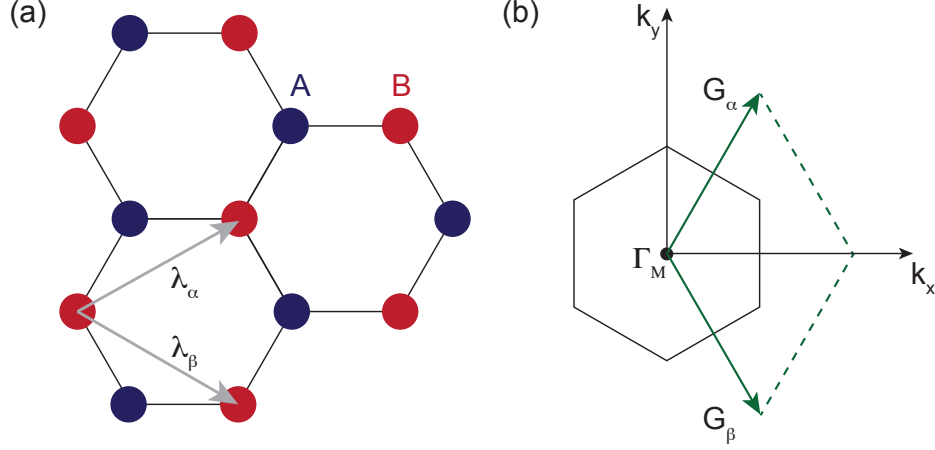


Figure S5. **Moiré lattice and its Brillouin zone.** (a) Real space lattice of the moiré lattice,  $\lambda_\alpha$  and  $\lambda_\beta$  are lattice unit vectors. (b) Brillouin zone with reciprocal lattice vectors  $\mathbf{G}_\alpha$  and  $\mathbf{G}_\beta$ .

#### S4. CALCULATION OF THRESHOLD DENSITY

The real-space lattice of bilayer graphene and hBN leads to a hexagonal moiré lattice (Fig. S5(a)). The lattice vectors can be written as:

$$\lambda_\alpha = \frac{\lambda}{2}(\sqrt{3}, 1), \quad \lambda_\beta = \frac{\lambda}{2}(\sqrt{3}, -1). \quad (\text{S3})$$

where  $\lambda$  is the moiré wavelength. The corresponding reciprocal lattice vectors are given by (Fig.S5(b)):

$$\mathbf{G}_\alpha = \frac{2\pi}{\sqrt{3}\lambda}(1, \sqrt{3}), \quad \mathbf{G}_\beta = \frac{2\pi}{\sqrt{3}\lambda}(1, -\sqrt{3}). \quad (\text{S4})$$

In the Uee scattering process, the condition for backscattering is

$$\mathbf{k}_1 + \mathbf{k}_2 = \mathbf{k}_3 + \mathbf{k}_4 + \mathbf{G} \quad (\text{S5})$$

here,  $\mathbf{k}_1, \mathbf{k}_2$  are the wave-vectors of the incoming electrons,  $\mathbf{k}_3, \mathbf{k}_4$  are the wave-vectors of the scattered electrons and  $\mathbf{G}$  is a reciprocal space lattice vector.

The lower limit on wave-vector  $k_t$  above which umklapp scattering is allowed comes from Eqn. S5, which gives  $k_t = G/4 = \pi/(\sqrt{3}\lambda)$ . The corresponding threshold carrier density above which Umklapp scattering starts can be written as  $n_t = |\mathbf{k}_t|^2/\pi = \pi/(3\lambda^2) = n_0\pi/(2\sqrt{3}) \approx 0.907n_0$ . (assuming an isotropic dispersion). Here,  $n_0 = 2/(\sqrt{3}\lambda^2)$  is the carrier density corresponding to one-fourth filling of moiré band.

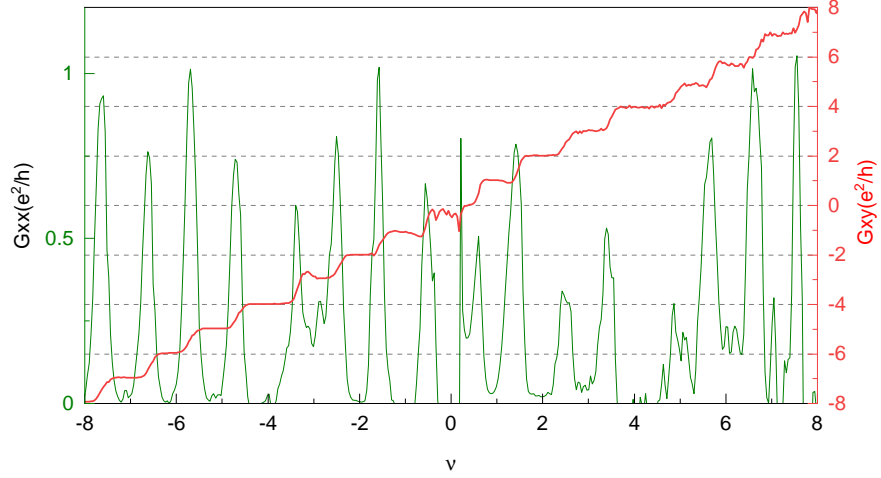


Figure S6. **Quantum Hall of the device.** Plots of  $G_{xx}$  (green solid line) and  $G_{xy}$  (red solid line) versus the filling factor  $\nu = nh/eB$ . The measurements were done for  $B = 5$  T and at  $T = 20$  mK.

## S5. QUANTUM HALL

The Quantum Hall measurements were performed to estimate the value of capacitance  $C_{bg}$  and  $C_{tg}$ . Fig.S6 shows  $G_{xx}$  (green solid line) and  $G_{xy}$  (red solid line) versus the filling fraction ( $\nu = nh/eB$ ) measured at perpendicular magnetic field of  $B = 5$  T. The appearance of the broken symmetry states establish that both spin and valley degeneracies are lifted, indicating the high quality of the device.



- 
- [1] N. W. Ashcroft and N. D. Mermin, Solid State Physics (Holt-Saunders, 1976).
- [2] M. Kaveh and N. Wiser, *Advances in Physics* **33**, 257 (1984).
- [3] M. Hideaki and F. Hidetoshi, *Journal of the Physical Society of Japan* **67**, 242 (1998).
- [4] J. R. Wallbank, R. Krishna Kumar, M. Holwill, Z. Wang, G. H. Auton, J. Birkbeck, A. Mishchenko, L. A. Ponomarenko, K. Watanabe, T. Taniguchi, K. S. Novoselov, I. L. Aleiner, A. K. Geim, and V. I. Falko, *Nature Physics* **15**, 32 (2019).
- [5] C. Mouldale and V. Fal'ko, *Phys. Rev. B* **107**, 144111 (2023).
- [6] H. Ishizuka and L. Levitov, *New Journal of Physics* **24**, 052001 (2022).
- [7] J. Bass, W. P. Pratt, and P. A. Schroeder, *Rev. Mod. Phys.* **62**, 645 (1990).
- [8] V. Gasparov and R. Huguenin, *Advances in Physics* **42**, 393 (1993), <https://doi.org/10.1080/00018739300101514>.
- [9] A. Messica, A. Soibel, U. Meirav, A. Stern, H. Shtrikman, V. Umansky, and D. Mahalu, *Phys. Rev. Lett.* **78**, 705 (1997).
- [10] Z. Fisk, H. R. Ott, T. M. Rice, and J. L. Smith, *Nature* **320**, 124 (1986).
- [11] A. H. MacDonald, R. Taylor, and D. J. W. Geldart, *Phys. Rev. B* **23**, 2718 (1981).
- [12] K. Behnia, *Annalen der Physik* **534**, 2100588 (2022), <https://onlinelibrary.wiley.com/doi/pdf/10.1002/andp.202100588>.
- [13] X. Lin, B. Fauqué, and K. Behnia, *Science* **349**, 945 (2015), <https://www.science.org/doi/pdf/10.1126/science.aaa8655>.
- [14] J. Wang, J. Wu, T. Wang, Z. Xu, J. Wu, W. Hu, Z. Ren, S. Liu, K. Behnia, and X. Lin, *Nature Communications* **11**, 3846 (2020).
- [15] D. van der Marel, J. L. M. van Mechelen, and I. I. Mazin, *Phys. Rev. B* **84**, 205111 (2011).
- [16] Y. Ando, S. Komiya, K. Segawa, S. Ono, and Y. Kurita, *Phys. Rev. Lett.* **93**, 267001 (2004).
- [17] D. L. Maslov and A. V. Chubukov, *Reports on Progress in Physics* **80**, 026503 (2016).
- [18] P. N. Trofimenkoff and J. W. Ekin, *Phys. Rev. B* **4**, 2392 (1971).
- [19] M. K. Jat, P. Tiwari, R. Bajaj, I. Shitut, S. Mandal, K. Watanabe, T. Taniguchi, H. R. Krishnamurthy, M. Jain, and A. Bid, Higher-order bragg gaps in the electronic band structure of bilayer graphene renormalized by recursive supermoiré potential (2023), [arXiv:2304.01720 \[cond-mat.mes-hall\]](https://arxiv.org/abs/2304.01720).

- [20] L. A. Ponomarenko, R. V. Gorbachev, G. L. Yu, D. C. Elias, R. Jalil, A. A. Patel, A. Mishchenko, A. S. Mayorov, C. R. Woods, J. R. Wallbank, M. Mucha-Kruczynski, B. A. Piot, M. Potemski, I. V. Grigorieva, K. S. Novoselov, F. Guinea, V. I. Fal'ko, and A. K. Geim, *Nature* **497**, 594 (2013).
- [21] M. Kuiri, S. K. Srivastav, S. Ray, K. Watanabe, T. Taniguchi, T. Das, and A. Das, *Phys. Rev. B* **103**, 115419 (2021).
- [22] Z. Wang, Y. B. Wang, J. Yin, E. Tovari, Y. Yang, L. Lin, M. Holwill, J. Birkbeck, D. J. Perello, S. Xu, J. Zultak, R. V. Gorbachev, A. V. Kretinin, T. Taniguchi, K. Watanabe, S. V. Morozov, M. Andelkovic, S. P. Milovanovic, L. Covaci, F. M. Peeters, A. Mishchenko, A. K. Geim, K. S. Novoselov, V. I. Falko, A. Knothe, and C. R. Woods, *Science Advances* **5**, eaay8897 (2019), <https://www.science.org/doi/pdf/10.1126/sciadv.aay8897>.
- [23] N. R. Finney, M. Yankowitz, L. Muraleetharan, K. Watanabe, T. Taniguchi, C. R. Dean, and J. Hone, *Nature Nanotechnology* **14**, 1029 (2019).
- [24] Y. Yang, J. Li, J. Yin, S. Xu, C. Mullan, T. Taniguchi, K. Watanabe, A. K. Geim, K. S. Novoselov, and A. Mishchenko, *Science Advances* **6**, eabd3655 (2020), <https://www.science.org/doi/pdf/10.1126/sciadv.abd3655>.
- [25] M. Yankowitz, J. Xue, D. Cormode, J. D. Sanchez-Yamagishi, K. Watanabe, T. Taniguchi, P. Jarillo-Herrero, P. Jacquod, and B. J. LeRoy, *Nature Physics* **8**, 382 (2012).
- [26] P. Tiwari, D. Sahani, A. Chakraborty, K. Das, K. Watanabe, T. Taniguchi, A. Agarwal, and A. Bid, *Nano Letters* **23**, 6792 (2023), pMID: 37477991, <https://doi.org/10.1021/acs.nanolett.3c00045>.
- [27] K. R. Amin, R. Nagarajan, R. Pandit, and A. Bid, *Phys. Rev. Lett.* **129**, 186802 (2022).
- [28] P. Tiwari, M. K. Jat, A. Udupa, D. S. Narang, K. Watanabe, T. Taniguchi, D. Sen, and A. Bid, *npj 2D Materials and Applications* **6**, 68 (2022).
- [29] D. R. Hofstadter, *Phys. Rev. B* **14**, 2239 (1976).
- [30] R. Krishna Kumar, A. Mishchenko, X. Chen, S. Pezzini, G. Auton, L. Ponomarenko, U. Zeitler, L. Eaves, V. Fal'ko, and A. Geim, *Proceedings of the National Academy of Sciences* **115**, 5135 (2018).
- [31] R. Huber, M.-N. Steffen, M. Drienovsky, A. Sandner, K. Watanabe, T. Taniguchi, D. Pfannkuche, D. Weiss, and J. Eroms, *Nature Communications* **13**, 2856 (2022).
- [32] Z. Wang, Y. B. Wang, J. Yin, E. Tóvári, Y. Yang, L. Lin, M. Holwill, J. Birkbeck, D. J. Perello, S. Xu, J. Zultak, R. V. Gorbachev, A. V. Kretinin, T. Taniguchi, K. Watanabe, S. V. Morozov, M. Anđelković, S. P. Milovanović, L. Covaci, F. M. Peeters, A. Mishchenko, A. K. Geim, K. S. Novoselov, V. I. Falko, A. Knothe, and C. R. Woods, *Science Advances* **5**, eaay8897 (2019),

- <https://www.science.org/doi/pdf/10.1126/sciadv.aay8897>.
- [33] Y. Nam, D.-K. Ki, D. Soler-Delgado, and A. F. Morpurgo, *Nature Physics* **13**, 1207 (2017).
- [34] A. Laitinen, M. Kumar, M. Oksanen, B. Plaçais, P. Virtanen, and P. Hakonen, *Phys. Rev. B* **91**, 121414 (2015).
- [35] H. Ochoa, E. V. Castro, M. I. Katsnelson, and F. Guinea, *Phys. Rev. B* **83**, 235416 (2011).
- [36] J.-H. Chen, C. Jang, S. Adam, M. S. Fuhrer, E. D. Williams, and M. Ishigami, *Nature Physics* **4**, 377 (2008).
- [37] A. B. Kashuba, *Phys. Rev. B* **78**, 085415 (2008).
- [38] W. G. Baber and N. F. Mott, *Proceedings of the Royal Society of London. Series A - Mathematical and Physical Sciences* **158**, 383 (1937), <https://royalsocietypublishing.org/doi/pdf/10.1098/rspa.1937.0027>.
- [39] Y. Xu, F. Herman, V. Granata, D. Destraz, L. Das, J. Vonka, S. Gerber, J. Spring, M. Gibert, A. Schilling, X. Zhang, S. Li, R. Fittipaldi, M. H. Fischer, A. Vecchione, and J. Chang, *Communications Physics* **4**, 1 (2021).
- [40] R. Hlubina, *Phys. Rev. B* **53**, 11344 (1996).
- [41] S. Koshino, *Progress of Theoretical Physics* **24**, 1049 (1960), <https://academic.oup.com/ptp/article-pdf/24/5/1049/5218931/24-5-1049.pdf>.
- [42] A. M. Seiler, F. R. Geisenhof, F. Winterer, K. Watanabe, T. Taniguchi, T. Xu, F. Zhang, and R. T. Weitz, *Nature* **608**, 298 (2022).
- [43] E. Jung, D. Park, and C.-S. Park, *Phys. Rev. B* **87**, 115438 (2013).
- [44] P. Tiwari, S. K. Srivastav, and A. Bid, *Phys. Rev. Lett.* **126**, 096801 (2021).
- [45] Y. Zhang, T.-T. Tang, C. Girit, Z. Hao, M. C. Martin, A. Zettl, M. F. Crommie, Y. R. Shen, and F. Wang, *Nature* **459**, 820 (2009).
- [46] E. Icking, L. Banszerus, F. Wörtche, F. Volmer, P. Schmidt, C. Steiner, S. Engels, J. Hesselmann, M. Goldsche, K. Watanabe, T. Taniguchi, C. Volk, B. Beschoten, and C. Stampfer, *Advanced Electronic Materials* **8**, 2200510 (2022), <https://onlinelibrary.wiley.com/doi/pdf/10.1002/aelm.202200510>.
- [47] T. Taychatanapat and P. Jarillo-Herrero, *Phys. Rev. Lett.* **105**, 166601 (2010).
- [48] Z. Zhu, S. Carr, Q. Ma, and E. Kaxiras, *Phys. Rev. B* **106**, 205134 (2022).
- [49] Z. He, C. Yu, Q. Liu, X. Song, X. Gao, J. Guo, C. Zhou, S. Cai, and Z. Feng, *Carbon* **164**, 435 (2020).
- [50] T. Uwanno, T. Taniguchi, K. Watanabe, and K. Nagashio, *ACS Applied Materials & Interfaces* **10**, 28780 (2018).

- [51] N. Hasan, U. Kansakar, E. Sherer, M. A. DeCoster, and A. D. Radadia, *ACS Omega* **6**, 30281 (2021).
- [52] N. Petrone, T. Chari, I. Meric, L. Wang, K. L. Shepard, and J. Hone, *ACS Nano* **9**, 8953 (2015).
- [53] S. Tang, H. Wang, Y. Zhang, A. Li, H. Xie, X. Liu, L. Liu, T. Li, F. Huang, X. Xie, and M. Jiang, *Scientific Reports* **3**, 2666 (2013).
- [54] S. Wang, J. Crowther, H. Kageshima, H. Hibino, and Y. Taniyasu, *ACS Nano* **15**, 14384 (2021).
- [55] A. Summerfield, A. Davies, T. S. Cheng, V. V. Korolkov, Y. Cho, C. J. Mellor, C. T. Foxon, A. N. Khlobystov, K. Watanabe, T. Taniguchi, L. Eaves, S. V. Novikov, and P. H. Beton, *Scientific Reports* **6**, 22440 (2016).
- [56] X. Sun, S. Zhang, Z. Liu, H. Zhu, J. Huang, K. Yuan, Z. Wang, K. Watanabe, T. Taniguchi, X. Li, M. Zhu, J. Mao, T. Yang, J. Kang, J. Liu, Y. Ye, Z. V. Han, and Z. Zhang, *Nature Communications* **12**, 7196 (2021).
- [57] R. K. Kumar, X. Chen, G. H. Auton, A. Mishchenko, D. A. Bandurin, S. V. Morozov, Y. Cao, E. Khestanova, M. B. Shalom, A. V. Kretinin, K. S. Novoselov, L. Eaves, I. V. Grigorieva, L. A. Ponomarenko, V. I. Fal'ko, and A. K. Geim, *Science* **357**, 181 (2017), <https://www.science.org/doi/pdf/10.1126/science.aal3357>.
- [58] B. Hunt, J. D. Sanchez-Yamagishi, A. F. Young, M. Yankowitz, B. J. LeRoy, K. Watanabe, T. Taniguchi, P. Moon, M. Koshino, P. Jarillo-Herrero, and R. C. Ashoori, *Science* **340**, 1427 (2013), <https://www.science.org/doi/pdf/10.1126/science.1237240>.
- [59] L. Wang, S. Zihlmann, M.-H. Liu, P. Makk, K. Watanabe, T. Taniguchi, A. Baumgartner, and C. Schönenberger, *Nano Letters* **19**, 2371 (2019), PMID: 30803238, <https://doi.org/10.1021/acs.nanolett.8b05061>.